

## Pattern formation in spatially forced thermal convection

This content has been downloaded from IOPscience. Please scroll down to see the full text.

2012 New J. Phys. 14 053010

(<http://iopscience.iop.org/1367-2630/14/5/053010>)

View [the table of contents for this issue](#), or go to the [journal homepage](#) for more

Download details:

IP Address: 134.76.162.165

This content was downloaded on 11/06/2014 at 09:50

Please note that [terms and conditions apply](#).

## Pattern formation in spatially forced thermal convection

**S Weiss**<sup>1,4</sup>, **G Seiden**<sup>1,5</sup> and **E Bodenschatz**<sup>1,2,3,6</sup>

<sup>1</sup> Max Planck Institute for Dynamics and Self-Organization (MPIDS),  
37077 Göttingen, Germany

<sup>2</sup> Institute for Nonlinear Dynamics, University of Göttingen, 37077 Göttingen,  
Germany

<sup>3</sup> Laboratory of Atomic and Solid-State Physics and Sibley School of  
Mechanical and Aerospace Engineering, Cornell University, Ithaca,  
NY 14853-2501, USA

E-mail: [eberhard.bodenschatz@ds.mpg.de](mailto:eberhard.bodenschatz@ds.mpg.de)

*New Journal of Physics* **14** (2012) 053010 (24pp)


Received 28 March 2011

Published 9 May 2012

Online at <http://www.njp.org/>

doi:10.1088/1367-2630/14/5/053010

**Abstract.** In this paper, we present experimental results on the interplay between two different symmetry breaking mechanisms in a pattern forming system, namely inclined layer convection (ILC) with a spatially modulated heated plate. By varying the relative strength and relative orientation, we explored in detail the interplay of these symmetry breaking mechanisms. We found a stabilization of spatio-temporal chaos and resonant interactions that led to superlattice patterns. The fundamental mechanisms observed should be equally applicable to other pattern forming systems.

 Online supplementary data available from [stacks.iop.org/NJP/14/053010/mmedia](http://stacks.iop.org/NJP/14/053010/mmedia)

<sup>4</sup> Current address: Department of Physics and Center for the Study of Complex Systems, University of Michigan, Ann Arbor, MI48109, USA.

<sup>5</sup> Current address: Department of Environmental Sciences and Energy Research, Weizmann Institute of Science, Rehovot 76100, Israel.

<sup>6</sup> Author to whom any correspondence should be addressed.

**Contents**

|  |           |
|--|-----------|
| <b>1. Introduction</b>   | <b>2</b>  |
| <b>2. Spatially forced inclined layer convection</b>                 | <b>3</b>  |
| <b>3. The experimental setup</b>                                     | <b>5</b>  |
| <b>4. Convection onset in the unforced reference cell</b>            | <b>7</b>  |
| <b>5. General features of the phase diagrams for the forced cell</b> | <b>7</b>  |
| <b>6. Patterns</b>   | <b>9</b>  |
| 6.1. The horizontal case ( $\theta = 0^\circ$ ) . . . . .            | 9         |
| 6.2. Small inclination angles . . . . .                              | 11        |
| 6.3. Intermediate inclination angles . . . . .                       | 13        |
| 6.4. Large inclination angles . . . . .                              | 16        |
| <b>7. Discussion and conclusion</b>                                  | <b>20</b> |
| <b>Acknowledgments</b>   | <b>22</b> |
| <b>References</b>  | <b>22</b> |

**1. Introduction**

Out-of-equilibrium patterns, such as for example in fluids and biological systems, as well as in social and economical contexts, often form by symmetry breaking bifurcations. While the detailed pattern forming processes in these spatially extended dynamical systems differ greatly, they often share generic underlying features that can be described by universal equations [1, 2]. For this reason, paradigm pattern forming systems, such as the thermal convection of a thin fluid layer, have been extensively investigated and have contributed significantly to our understanding (see e.g. [3]).

While most studies concern isotropic systems, naturally driven pattern forming systems often contain additional, externally imposed symmetry breaking mechanisms that affect the patterns and their dynamics. Frost heave phenomena leading to stone–soil separation in alpine and polar regions [4] and banded vegetation in arid areas [5] are two examples, where the strength of the anisotropy (i.e. the sloped ground) determines the observed patterns. Atmospheric convection over topography [6] and fingerprint formation in the presence of normal epidermic displacements [7] are other examples.

Spatially periodic forcing is well suited for exploring the interaction between externally imposed symmetries and intrinsic symmetries preferred by the system. In the past, a variety of one-dimensional spatial forcing techniques have been applied to different pattern forming systems. Busse and Whitehead [8] used optically induced, spatially modulated heat deposition in Rayleigh–Bénard convection of water and investigated the stability of convection rolls. Lowe and Gollub [9] used a spatially modulated electrode in electro convection of nematic liquid crystals and studied commensurate–incommensurate transitions. In recent experiments, Míguez *et al* observed the effect of forcing on a two-dimensional (2D) Turing pattern [10]. They illuminated the chlorine dioxide–iodine–malonic acid reaction–diffusion system with a translating quasi-1D-light pattern and observed a variety of steady and dynamical hexagonal patterns as a function of the forcing parameters. Dolnik *et al* [11] used the same system but applied a steady forcing in the form of a 2D hexagonal pattern. Depending on the forcing

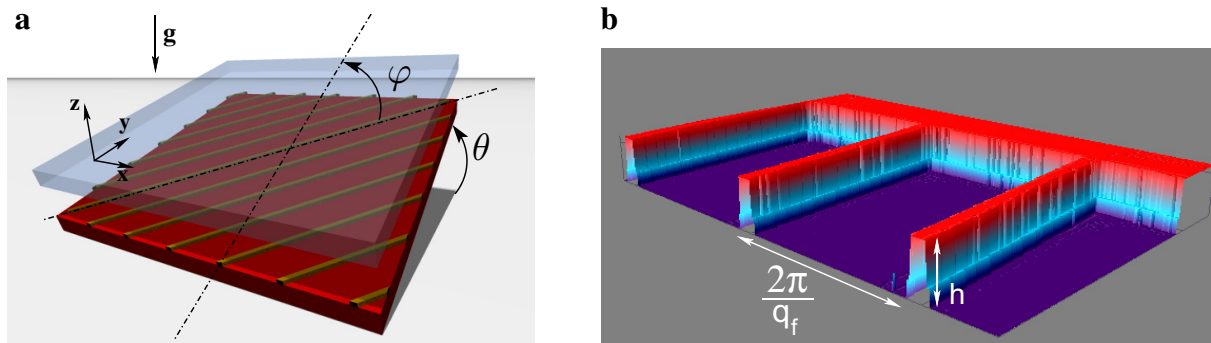


**Figure 1.** (a) Schematic diagram of forced ILC. Shown are the inclination angle  $\theta$  and the angle  $\varphi$  between the in-plane gravity component and the SU-8 ridges. (b) Surface structure of the warm plate, as measured with white light interferometry.

wavenumber, their system adopted either the forcing pattern or a hexagonal superlattice pattern [12]. McCoy *et al* [13] used 1D surface corrugations on the bottom plate to force a Rayleigh–Bénard convection system. They found novel coherent phase-kink structures that still await a theoretical explanation.

In this paper we report experiments on a quasi-1D, spatial periodically forced pattern forming system that by itself has a broken rotational symmetry. The system is inclined layer convection (ILC), where a thin fluid layer is heated on one side and cooled on the other and which is inclined with respect to gravity [3, 14]. Microfabricated periodic surface corrugations on the heated plate (see figure 1(b)) are used to break an additional symmetry [13, 15–17]. Some results were published earlier [16], and here we report a detailed study, for which both the relative orientation and the relative strength of both symmetry breaking mechanisms were systematically varied [17].

The paper is organized as follows. In section 2 we define the system and in section 3 we describe the experimental setup. In section 4 we present measurements of the convection onset in the unforced reference cell. In section 5 we show the phase diagrams for the three different forcing cases and explain the general features of them. The observed patterns are discussed in detail in section 6. We summarize and discuss our results in section 7.

## 2. Spatially forced inclined layer convection

Thermal convection in a thin horizontal fluid layer of thickness  $d$  confined by two parallel plates is a generic and by now the most investigated isotropic pattern forming system [3]. If the driving buoyancy due to the destabilizing temperature gradient is stronger than the damping effects by viscosity and thermal diffusion, convection sets in and breaks the rotational symmetry of the system. The degree to which the system is thermally driven, i.e. the ratio between the driving and the damping forces, is given by the Rayleigh number:  $Ra = g\alpha\Delta Td^3/\kappa\nu$ . Here,  $\Delta T$  is the temperature difference between the two plates,  $\nu$  is the kinematic viscosity of the fluid and  $\alpha$  and  $\kappa$  are its thermal expansion coefficient and its thermal diffusivity. Above a critical temperature difference (i.e. a critical Rayleigh number  $Ra_c$ ) convection sets in as parallel rolls of arbitrary lateral orientation. The other non-dimensional parameter, which measures the relative strength of the nonlinearity in the momentum equation versus that of the heat equation, is the Prandtl

number:  $Pr = \nu/\kappa$ . Here we used compressed  $\text{CO}_2$  with  $Pr = 1.3$ , for which in the horizontal case bistability between spiral defect chaos and straight ideal rolls was observed in the weakly nonlinear regime [14].

When the fluid layer is inclined at an angle  $\theta$  with respect to gravity (figure 1), a large-scale shear flow (LSF) is created for any finite  $\Delta T$  with the warm (cold) fluid rising (falling) at the heated (cooled) plate. This flow breaks the rotational symmetry by singling out the direction along the in-plane gravity component. For fluids of  $Pr > 0.26$  a codimension two point between longitudinal and transverse rolls (TR) exists at an inclination angle  $\theta_{\text{cd}}$ . For angles  $\theta < \theta_{\text{cd}}$  convection sets in as longitudinal rolls (LR) aligned with their axis parallel to the inclination direction [18]. By using only the component of gravity normal to the fluid layer one can define a new Rayleigh number  $\tilde{Ra}(\theta) = Ra \cdot \cos \theta$ . It was shown that with this rescaling the convection onset for LR is independent of  $\theta$  at  $\tilde{Ra}_c = 1708$  for all  $\theta < \theta_{\text{cd}}$  (see, e.g., [19, 20]). Calculations of the critical wave number at onset of LR yield a value  $q_c^L = 3.117/d$ , which is also independent of  $\theta$  (see also figure 2 and the following section).

Above the inclination angle  $\theta_{\text{cd}}$ , which strongly depends on  $Pr$ , TR set in at lower Rayleigh numbers than LR and thus are the first instability. In contrast to the buoyancy driven LR, TR are driven by the instability of the cubic shear flow velocity profile (i.e. the LSF) and occur even when an inclined fluid layer is heated from above. The onset of TR cannot be calculated analytically, but a numerical approach such as a Galerkin method [3] has to be used. The critical wavenumber for TR depends on  $\theta$  and for  $Pr = 1.3$  at  $\theta = \theta_{\text{cd}} = 79.9^\circ$  is  $q_c^T = 2.817/d$ , which is smaller than  $q_c^L = 3.117/d$  (see figure 2(b)).

In our investigation, we applied a periodic surface modulation in the form of long rectangular ridges to the heated plate. This modulation influences both the temperature and the velocity field (through the boundary conditions) and thus forces the convection patterns. The forcing can be characterized by three additional parameters: the forcing wave number  $q_f$ , the orientation of the modulation with respect to the inclination direction  $\varphi$  and the forcing amplitude  $\delta = a_1 h/d$  [16, 21]. Here  $a_1$  is the coefficient of the leading Fourier mode in the decomposition of the rectangular modulation profile and  $h$  is the height of the corrugation (see figure 1). In the experiments presented here, both  $q_f$  and  $\delta$  were kept fixed;  $q_f$  was chosen in the vicinity of the critical wave number of longitudinal rolls  $q_c^L$ . As shown in [16], the approximation of the surface texture by only the first Fourier mode appears to be sufficient if the convection strength is small, i.e. close to onset. We expect that with increasing convection strength, this approximation is no longer valid and in a theoretical analysis higher order modes have to be considered. It is thus very likely that for large convection strength the observed pattern will depend to some extent on the exact shape of the surface modulation.

Forced ILC can serve as a paradigm for a pattern forming system for which two externally broken symmetries can be *independently* tuned. The 3D parameter space is spanned by two geometrical degrees of freedom, namely the inclination angle  $\theta$  and the forcing angle  $\varphi$ , and also by the reduced temperature difference, defined as  $\varepsilon = \Delta T/\Delta T_c(\theta) - 1$ , where  $\Delta T_c(\theta)$  is the critical temperature difference at which convection sets in for unforced ILC.

In this paper we report experiments with forcing angles that correspond to the most generic symmetries for lattice patterns:  $\varphi = 0^\circ$  (parallel stripes),  $60^\circ$  (hexagons) and  $90^\circ$  (squares). In the following, the corresponding forcing cases will also be referred to as the longitudinal, oblique and transverse forcing cases.

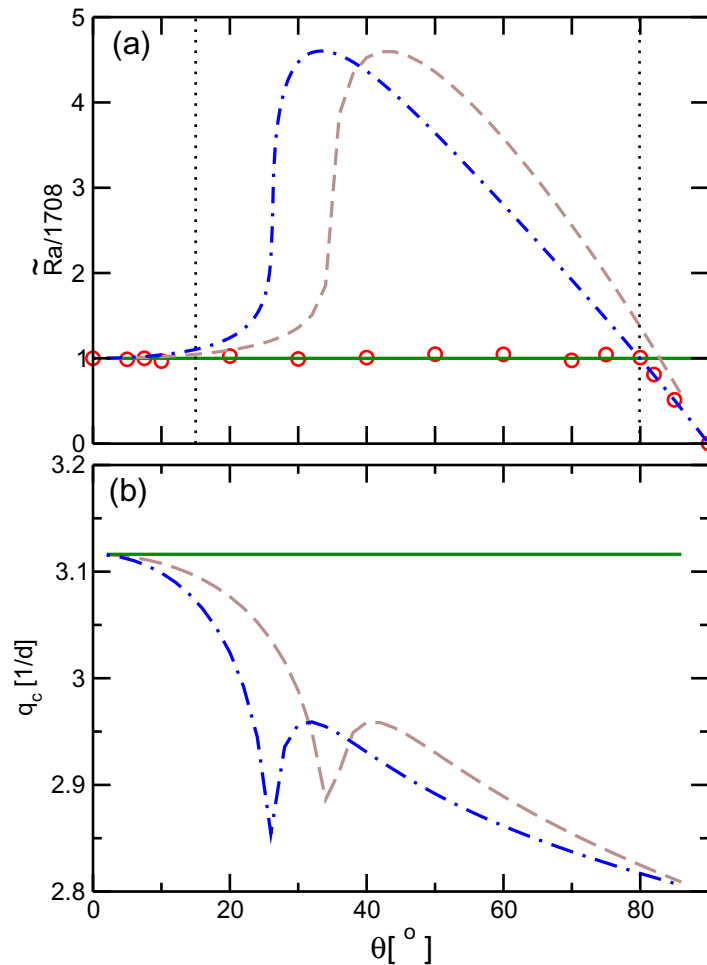


**Figure 2.** (a) Measured convection onset in the unforced reference cell as a function of  $\theta$  (red circles) and numerically calculated onset for rolls with angles  $\psi = 0$  (solid green curve),  $\psi = 90^\circ$  (point-dashed blue curve) and  $\psi = 60^\circ$  (dashed brown curve).  $\psi$  gives the angle of the roll axis with the in-plane gravity component. The dotted vertical line at  $\theta = 15^\circ$  marks an arbitrary chosen boundary between the low and moderate inclination regions as described in the text. The second dotted vertical line at  $79.9^\circ$  marks the critical angle  $\theta_{cd}$  above which TR first become unstable. (b) Numerically calculated critical wave numbers  $q_c$  for rolls with angles  $\psi = 0$  (solid green curve),  $\psi = 90^\circ$  (point-dashed blue curve) and  $\psi = 60^\circ$  (dashed brown curve). These plots are for experimental conditions with  $Pr = 1.3$ . Similar curves for  $Pr = 1.0$  have already been published in [25].

### 3. The experimental setup

We used  $\text{CO}_2$  gas at  $(48.2 \pm 0.07)$  bar as the convecting fluid. Compressed gases allow investigation of shallow layers with large width to height ratios under Boussinesq conditions and with time scales short enough for the investigation of non-transient states [3, 22]. The

convection cell consisted of two 1 cm thick cylindrical plates of 10 cm diameter. The cold plate was made of single crystalline sapphire and the warm plate was a single crystal of silicon. Both plates had a thermal conductivity at least 1000 times higher than that of the gas and can therefore be considered to be perfectly conducting. The transparent sapphire (cooled) and the mirror finish silicon (heated) plate allowed investigation of the patterns via shadowgraphy [23]. Both plates were aligned parallel to within  $0.6 \mu\text{m}$ , as measured by interferometry. The distance between the plates was  $d = (540 \pm 3) \mu\text{m}$ , as determined from the onset of convection in an unforced reference cell. The cold plate was cooled by a temperature-controlled water bath and the warm plate was heated with an electric film heater. A temperature difference  $\Delta T$  was set between the plates, and the temperature of each plate was held constant to within  $\pm 0.4 \text{ mK}$ . In all experiments, the average temperature was set to  $T_{\text{av}} = (25.00 \pm 0.01) ^\circ\text{C}$ , resulting in  $Pr = 1.30$ . The thermal vertical diffusion time under these conditions is  $\tau_\kappa = d^2/\kappa = 2.8 \text{ s}$ .

A quasi-1D periodic forcing was introduced by texturing the warm plate with lithographically produced SU-8 ridges (see [15, 17]). The ridge height was  $(65 \pm 3) \mu\text{m}$  and the width was  $(100 \pm 3) \mu\text{m}$  as measured with a white light interferometer. The periodicity was  $\lambda_f = 2\pi/q_f = 1 \text{ mm}$  (figure 1(b)). For the cell heights used here the forcing wave number  $q_f$  was close to the critical wave number for LR  $q_c^L = 3.117/d = 0.92 q_f$ . An exact match of  $q_f$  and  $q_c$  could not be easily achieved due to experimental constraints. The forcing with SU-8 had two effects. On the one hand, this corrugation introduced a periodic height variation and, on the other hand, it introduced a periodic horizontal temperature variation. In the case of a horizontal fluid layer, Seiden *et al* [16] have shown that the effect of the SU-8 structure can be matched to a periodic variation of the temperature of the warm plate.

The side walls were cut out of paper sheets in order to optimally match the thermal properties of the gas and to avoid stationary as well as transient side wall forcing at the lateral boundaries [24]. The paper sheets were of circular shape with a diameter of 10 cm in order to fully cover the warm plate. Two square convection cells with a side length of  $L = 85d$  and  $35d$  were cut into the paper. The open space of the larger cell was placed above the lithographically fabricated surface corrugations on the warm plate (figure 1(b)), while the smaller one was positioned over the unstructured area of the warm plate and served as a reference. In all experiments, the side walls were aligned so that one side was parallel to the in-plane gravitational component, allowing a 1D LSF.

The shadowgraph technique (see [23]) was used to capture the 2D structure of the temperature field. Cold areas of the fluid lead to a higher intensity and appear bright in the images, while warm fluid areas appear dark. Images were recorded via a CCD camera (QImaging®—QICam B) and image processed. For all convection patterns shown here, the in-plane gravity component pointed downwards.

During a typical experimental run,  $\theta$  and  $\varphi$  were held constant and  $\Delta T$  was increased in small steps. After each temperature change, sufficient time was given for the system to reach a steady state (at least 100 thermal diffusion times) before images of the convection state were taken. Typical temperature differences in the experiment ranged from  $\Delta T = 1.29 \text{ K}$  for the convection onset in the reference cell at  $\theta = 0^\circ$  to  $\Delta T = 9.0 \text{ K}$  for  $\theta = 85^\circ$  where longitudinal bursts (LB) start to appear. For the latter, the Busse parameter [3] was  $Q_{\text{Busse}} = 3.26$ , indicating that the Boussinesq approximation may not be sufficient for describing this system.

#### 4. Convection onset in the unforced reference cell

Figure 2(a) shows the measured onset of convection in the unforced reference cell as a function of the inclination angle  $\theta$ . The experimental data are marked by red circles, the green solid line is the theoretically predicted onset of LR, the blue dashed-point line of TR and the brown dashed line of oblique rolls, i.e. rolls with an angle  $\psi = 60^\circ$  to the in-plane gravity component. The blue and the brown curves were calculated numerically for  $Pr = 1.30$  by using a Galerkin code provided by Werner Pesch of the University of Bayreuth, Germany [25]. Similar curves for  $Pr = 1.0$  were reported in [25].

The experimental data agree well with the Galerkin data; in particular, the experimentally observed critical inclination angle  $\theta_{cd}^{\text{exp}} = (80.1 \pm 0.4)^\circ$  agrees well with the theoretical value  $\theta_{cd}^{\text{theo}} = 79.9^\circ$ . In figure 2, one can roughly distinguish three different regions of inclination angles (separated by vertical dotted lines): (i) a low inclination region ( $0^\circ \leq \theta \lesssim 15^\circ$ ), where the calculated onset for all three curves is close to  $\tilde{Ra}_c = 1708$ ; (ii) a moderate inclination region, where the calculated onset for rolls with  $\psi \neq 0$  increases strongly, reaches a maximum and decreases again; and (iii) a large inclination region for  $\theta > \theta_{cd}$  where TR are the linear instability of the base state. We note that the value of  $\theta$  for which these onset curves have a maximum is smallest for transversal rolls ( $\psi = 90^\circ$ ) and increases for decreasing  $\psi$  (see also [17, 25]).

The same three regions of inclination angles can also be seen in the phase diagrams corresponding to the forced cell (figure 3). Therefore, section 5 is divided into subsections, each describing a different  $\theta$  region. Note that the exact  $\theta$  range of each region varies with  $\varphi$  and is therefore given by pattern boundaries rather than the exact vertical dotted lines in figure 2.

In order to better understand the observed patterns, we show in figure 2(b) the Galerkin-calculated critical wave numbers for parallel rolls with  $\psi = 0$  (solid green),  $90^\circ$  (point-dashed blue) and  $60^\circ$  (dashed brown). The critical wave number of longitudinal rolls  $q_c^L = 3.117$  is identical to  $q_c$  of the horizontal configuration. The other  $q_c$ -curves are lower than  $q_c^L$ , but do not show a monotonic decrease with  $\theta$ . Instead, they show a sharp minimum and a smooth maximum. It is interesting to note that the minima of the  $q_c$ 's appear at inclination angles at which  $\tilde{Ra}_c(\theta)$  has its largest increase, while their maxima are when  $\tilde{Ra}_c$  is maximal. One might speculate that the sharp minimum corresponds to a transition from a buoyancy-induced instability to a shear-driven one.

#### 5. General features of the phase diagrams for the forced cell

We now proceed to the exploration of the  $\theta$ - $\varepsilon$ -phase space for the three different forcing angles  $\varphi$ . Note that the control parameter here is defined most conveniently as  $\varepsilon = \Delta T / \Delta T_c(\theta) - 1$ , where  $\Delta T_c(\theta)$  is the temperature difference at convection onset in the reference cell. In the horizontal case, the experimentally observed convection onset in the reference cell was at  $\Delta T_c = 1.29$  K. This value increased with increasing inclination as shown in figure 2.

The phase diagrams for forced convection at  $\varphi = 0^\circ$ ,  $\varphi = 60^\circ$  and  $\varphi = 90^\circ$  are shown in figure 3. In all three cases a purely conducting state was not observed. Instead, steady straight rolls occur at any positive  $\Delta T$  ( $\varepsilon > -1$ ). The amplitude of these forced rolls grew with increasing  $\varepsilon$ , following an imperfect bifurcation [16]. For all  $\varphi$ , the forced rolls were phase-locked to the SU-8 structure and therefore had a wave vector  $\mathbf{q}_0 = \mathbf{q}_f$ , with  $\mathbf{q}_f$  being the wave vector of the periodic SU-8 structure (see figure 3). The blue solid circles mark the region beyond which forced rolls first became unstable. Note that the phase diagrams in figures 3(a)



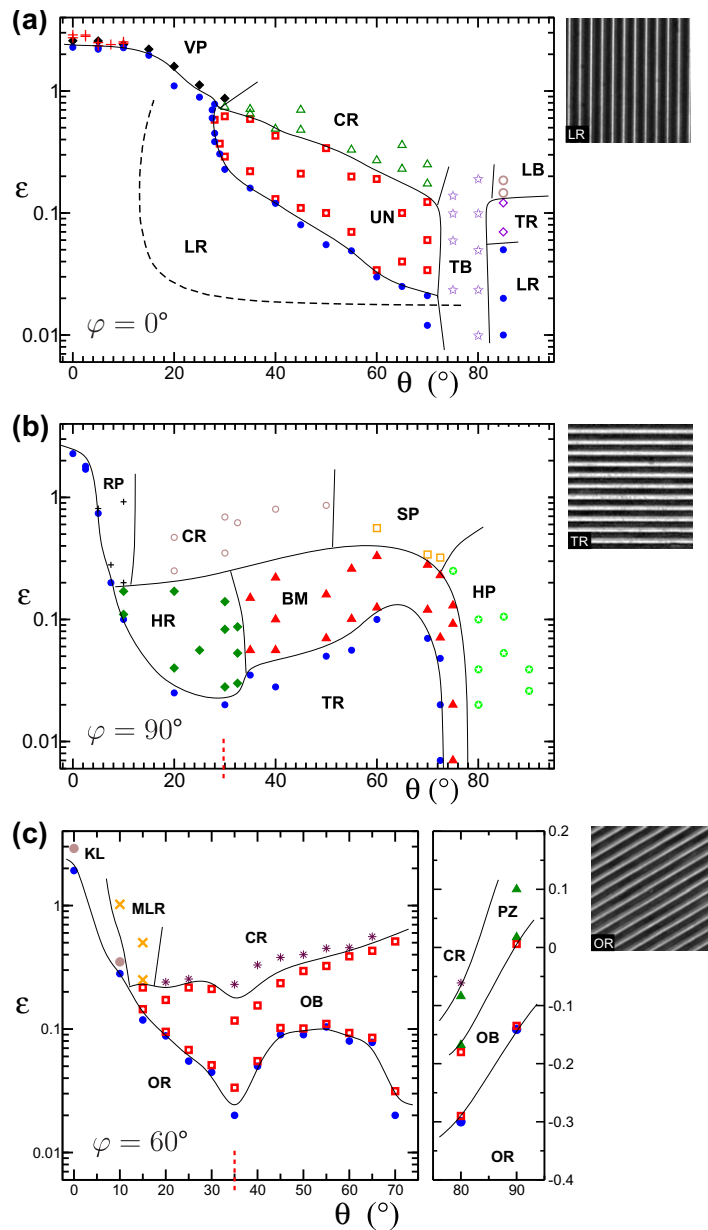


**Figure 3.** Phase diagrams for SU-8 ridges aligned parallel to gravity (a), perpendicular to gravity (b) and with an angle of  $\varphi = 60^\circ$  to gravity (c). Symbols mark places where different patterns are observed. Solid lines are hand-drawn instability lines that are a guide to the eyes. Straight roll patterns are marked in each phase diagram with blue solid circles. Images of these patterns are shown next to each phase diagram. For small angles, several patterns coexist for  $\varphi = 0^\circ$ . These patterns are all marked with red pluses. The dashed line in (a) marks the calculated instability line for LR in the unforced ILC. The red dashed lines in (b) and (c) mark the inclination angle at which the instability line of forced rolls has its minimum. Note that in (c) the  $\varepsilon$ -axis is logarithmic for small inclination angles (left part) but linear for large inclination angles (right part). Abbreviations are explained in the text.

and (b) have a logarithmic ordinate and thus show only positive values of  $\varepsilon$ . Therefore, the line at which forced rolls became unstable is not shown for large  $\theta$ , since the instability already occurred for  $\Delta T \lesssim \Delta T_c(\theta)$ . We now point out general features before we describe the patterns of each phase diagram in detail.

For the longitudinal forcing case ( $\varphi = 0$ , figure 3(a)), the instability line that separates LR at lower  $\varepsilon$  and undulations (UN; see [26]) at higher  $\varepsilon$  decreases monotonically with increasing  $\theta$  for  $\theta < \theta_{cd}$ . For comparison, the calculated instability of LR in unforced ILC is plotted as a dashed line in figure 3(a). It is significantly lower, implying that forcing *stabilizes* LR and suppresses the transition to UN in this  $\theta$  range (see [26]).

For the transverse ( $\varphi = 90^\circ$ ) and oblique ( $\varphi = 60^\circ$ ) forcing cases (figures 3(b) and (c)), the instability lines of forced rolls show the same behavior. They decrease with increasing  $\theta$  and reach a first minimum at inclination angles  $\theta \cong 30^\circ$  and  $\theta \cong 35^\circ$ , respectively (red vertical dashed lines in figures 3(b) and (c)). These minima correspond to the maxima of the onset curves associated with transverse and oblique rolls in the unforced case ( $\theta = 32^\circ$  and  $\theta = 42^\circ$ , see figure 2). As in figure 2, we can distinguish three regions.

(i) At low inclination ( $\theta \lesssim 15^\circ$ ), the LSF is relatively weak since its strength is proportional to  $\tan(\theta)$  [27]. The forced rolls become unstable at relatively high  $\varepsilon$  either to steady varicose pattern (VP) and rhombic pattern (RP) or to localized dynamical structures (kinks).

(ii) At moderate inclination angles ( $15^\circ \lesssim \theta < \theta_{cd}$ ), forced rolls become unstable to patterns that consist of not more than two modes in addition to  $\mathbf{q}_0$ . These are UN for  $\varphi = 0^\circ$ , hexarolls (HR) and bimodals (BM) for  $\varphi = 90^\circ$ , as well as another oblique bimodal pattern (OB) for  $\varphi = 60^\circ$ . All these patterns are steady at onset and show slow dynamics with increasing  $\varepsilon$ .

(iii) At large inclination angles ( $\theta > \theta_{cd}$ ), forced rolls become unstable at relatively low  $\varepsilon$  to complex spatio-temporal states. These include localized transverse bursts (TB) and LB for longitudinal forcing and superlattice patterns (scepter (SP), heart (HP) and pretzel (PZ)) for transverse and oblique forcing. We note that localized TB and LB are also observed for unforced ILC [18, 28].

## 6. Patterns

In sections 6.1–6.4, we review in detail the different states and the corresponding dynamics observed in the horizontal case and the three inclination angle regimes.

### 6.1. The horizontal case ( $\theta = 0^\circ$ )

Straight rolls became unstable to a steady *varicose pattern* (VP) when the control parameter was increased above  $\varepsilon \approx 2.4$  (figure 4(a)). As shown in figure 4(d), VPs are forced rolls, periodically phase modulated with the two symmetric modes:  $\mathbf{q}_1 = q_f(0.5, 0.35)$  and  $\mathbf{q}_2 = q_f(0.5, -0.35)$ . The modulation of adjacent rolls is thus  $180^\circ$  out of phase. Note that at this relatively large value of  $\varepsilon$ ,  $q_f$  lies outside the (unforced) Busse balloon [29] and thus straight rolls with this wavelength would be unstable in the unforced system. As shown in figure 4(d), the wave numbers form a resonant triad with  $\mathbf{q}_0 = \mathbf{q}_1 + \mathbf{q}_2$ . Such triad conditions are common in pattern forming systems. An example where these triad conditions were studied in detail is the case of Faraday waves that are forced with multiple frequencies [30, 31].

A further increase in  $\varepsilon$  led to stronger phase modulation until, at approximately  $\varepsilon \approx 2.7$ , two adjacent rolls came sufficiently close to merging and produced a localized jump of  $2\pi$  in

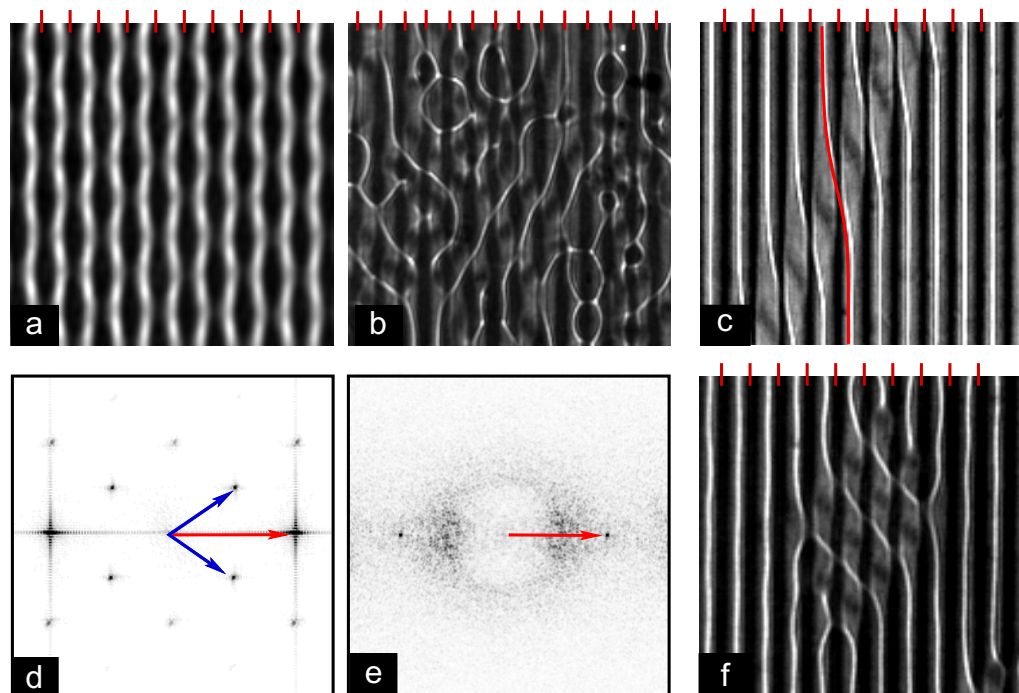


**Figure 4.** Varicose patterns and their corresponding Fourier transform at  $\theta = 0^\circ$  and  $\varepsilon = 2.7$  (a), (d). Spatio-temporal chaos at  $\theta = 0^\circ$  and  $\varepsilon = 2.66$  and its Fourier transform (b), (e). A single coherent kink line at  $\theta = 5^\circ$  and  $\varepsilon = 2.42$  (c) and a cluster of kinks at  $\theta = 0^\circ$  and  $\varepsilon = 1.69$  (f). The red lines at the top of each image mark the location of SU-8 ridges. The red arrow in the Fourier transforms marks the forcing wave vector  $\mathbf{q}_0$ , whereas the blue arrows stand for the instability modes  $\mathbf{q}_1$  and  $\mathbf{q}_2$ . See the movies of kinks (movie 1) and spatio-temporal chaos (movie 2) in the supplementary material available from [stacks.iop.org/NJP/14/053010/mmedia](http://stacks.iop.org/NJP/14/053010/mmedia)

the phase of the roll pattern, a so-called *kink defect* (see also [13] and below for a more detailed description). A single defect is not stable in this regime and the whole pattern turns abruptly into a spatio-temporal chaotic state (figure 4(b)), similar to the one reported by McCoy [15]. It is interesting that the Fourier transform of this state shows a diffuse ring with an average wave number of roughly  $0.5 q_f$  (figure 4(e)).

We also wish to note that in this  $\varepsilon$  range, the system realized two stable states. Varicose patterns only emerged when  $\varepsilon$  was increased from a state of straight rolls. On lowering  $\varepsilon$  below 2.7 from the state of spatio-temporal chaos, the system entered a state of crystalline kink chaos, which has been reported by McCoy [15]. This state consists of kinks that travel along the SU-8 ridges and align to straight lines or *kink clusters* as shown in figures 4(c) and (f). The number of kinks reduced continuously with decreasing  $\varepsilon$  and the system returned to perfect straight rolls at  $\varepsilon \approx 1.4$ . Even though McCoy used a very similar experimental setup, he observed VPs only as a transient state [15] during a rapid increase of  $\varepsilon$ . We believe that this can be attributed to the circular cell used in their experiment.

## 6.2. Small inclination angles

*Longitudinal forcing* ( $\varphi = 0^\circ$ ): When the cell is slightly inclined so that the SU-8 ridges are parallel to the in-plane gravity component, both the LSF and the SU-8 corrugations select LR. The instability line of LR decreases only slightly with increasing inclination angle  $\theta$ . Up to an inclination angle of  $\theta = 28^\circ$ , the straight LR were unstable to the VP, as in the horizontal case ( $\theta = 0$ ).

Whereas for small inclination angles ( $\theta < 7^\circ$ ) the VP were steady, as the underlying LSF intensified due to an increasing inclination angle, an increasing uphill drift was observed. For example, at  $\theta = 10^\circ$  and  $\varepsilon = 2.3$ , the VP drifted with a velocity of  $v_d \approx 0.5 d/\tau_\kappa$ . It is worth noting that at the same region of the  $\varepsilon$ - $\theta$ -phase diagram of the unforced ILC, subharmonic oscillations were observed, consisting of the same modes as those building the VP, but with different phase relations (see [18, 25, 27]). One might therefore interpret the VP state as a stabilized version of subharmonic oscillations. In the following we will see other instances where the forced system produces stabilized states that strongly resemble spatio-temporal chaotic states found in the unforced ILC cell.

For inclination angles  $\theta < 10^\circ$ , VPs were observed to coexist with coherent *kink lines* (KL; figure 4(c)). A single kink can be viewed as a localized  $2\pi$  phase jump [13]. With increasing  $\varepsilon$ , at the onset of KL we observed only one such phase jump per roll. The kinks of different rolls organized themselves to form a line of kinks obliquely across the entire cell (see movie 1 in the supplementary material (available from [stacks.iop.org/NJP/14/053010/mmedia](http://stacks.iop.org/NJP/14/053010/mmedia))). These oblique KL were mostly straight, but tended to bend towards the side walls. The KL drifted slowly downhill with a drift velocity of  $v_d \approx 1.59 d/\tau_\kappa$  (for  $\theta = 5^\circ$  and  $\varepsilon = 2.42$ ). The drift velocity increased with intensified LSF (increasing  $\varepsilon$  and/or  $\theta$ ). As  $\varepsilon$  increased further, shorter KL occurred that move independently across the cell. Several KL can move together and, depending on their orientation, they either annihilate or cluster to form a crystalline structure (figure 4(f)). This clustering phenomenon is similar to that reported by McCoy *et al* [13] for the horizontal configuration.

*Transverse forcing* ( $\varphi = 90^\circ$ ): In the transverse forcing case the two externally imposed constraints have competing effects. Transverse rolls (TR), which are phase-locked with the SU-8 structure at small  $\varepsilon$ , are destabilized by the LSF. In the range  $0^\circ < \theta < 10^\circ$ , TR are unstable to a rhombic pattern (RP) (figure 5(a)) with the wave vectors  $\mathbf{q}_0$  and  $\mathbf{q}_1$ . We note that  $\mathbf{q}_1$  depends on  $\varepsilon$  and changes from  $\mathbf{q}_1 = q_f(0.78, 0.45)$  at  $\varepsilon = 0.25$  to  $\mathbf{q}_1 = q_f(0.83, 0.15)$  at  $\varepsilon = 0.5$ . In the latter case, RP took the form of modulated straight rolls that were only  $10^\circ$  inclined to the in-plane gravity component. This is an indication that the RP pattern is topologically very similar to the *bimodal pattern* (BM) observed both for unforced ILC (close to  $\theta_{cd}$ , see [18]) and in the transverse forcing case for moderate inclination angles (see the following subsection). Both RP and BM occurred when in the unforced system LR and TR have similar onsets. As shown in figure 2, this is the case at very small  $\theta$  and close to the codimension two point  $\theta_{cd}$ .

The transition from TR to RP as  $\varepsilon$  increased did not occur globally (everywhere at the same time) but rather by domain spreading. Often, RP appeared first at the cell boundary or at an imperfection of the SU-8 texture and then spread over the whole cell. An example is shown in figure 5(b). Right at the domain boundary, the transition from TR to RP appeared in two steps. At first, TR became unstable to VPs with wave vectors  $\mathbf{q}_{1,2} \approx q_f(\pm 0.5, 0.5)$  (figure 5(b) at  $t = 0$ ). This is very similar to the transients observed when LR were unstable to KL for longitudinal forcing at small inclination angles. Here too, the VPs evolved into patches of

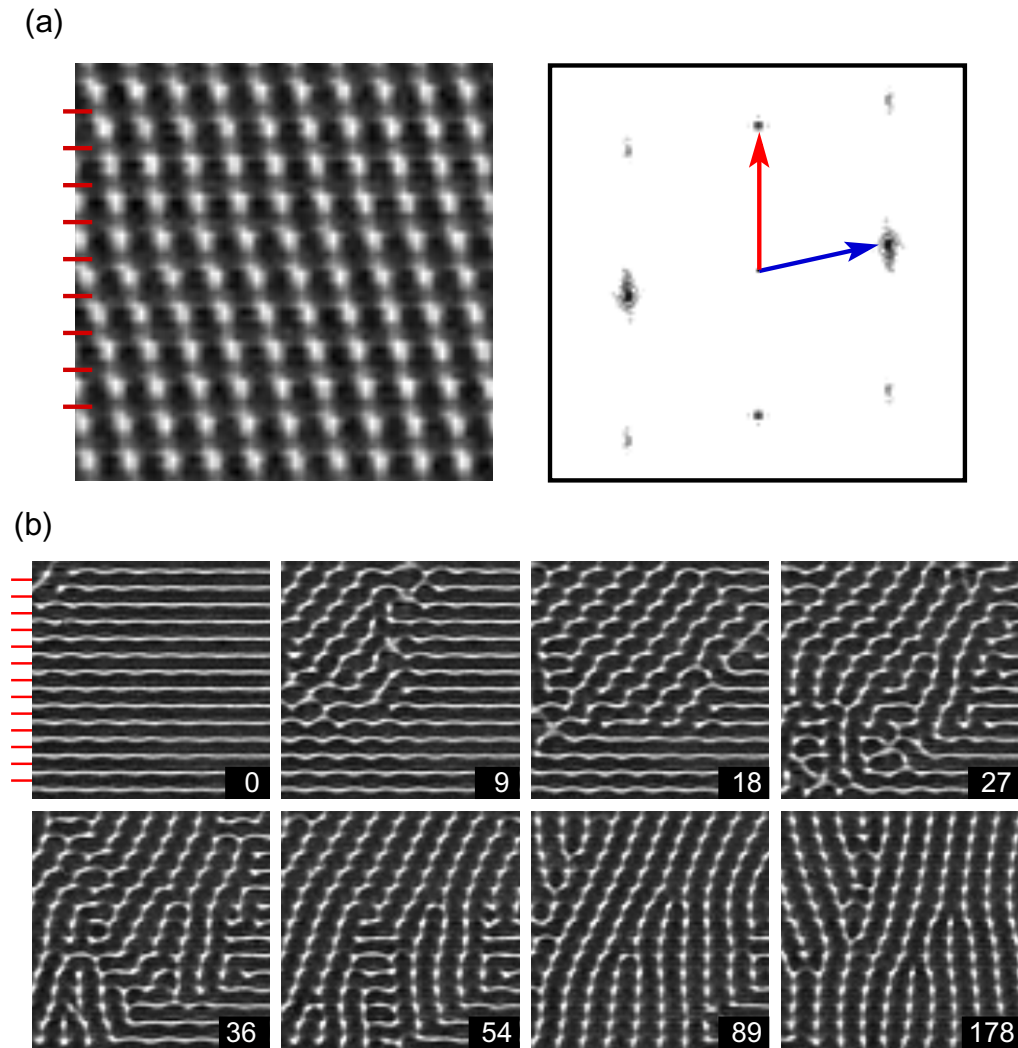


**Figure 5.** (a) Typical RP and its Fourier transform (taken at  $\theta = 10^\circ$ ,  $\varepsilon = 0.23$ ). The red arrow marks  $\mathbf{q}_0$  and the blue arrow marks  $\mathbf{q}_1$ . (b) Evolution of RP with time at very small inclination angles. Images taken at  $\theta = 5^\circ$  and  $\varepsilon = 0.81$ . The numbers in the corner of each image are the times in units of  $\tau_\kappa$  at which the image was taken. The state after  $178 \tau_\kappa$  is the final stable state of the system. The red horizontal lines in the first images of (a) and (b) mark the locations of the SU-8 stripes.

kink-clusters through the merging of adjacent modulated rolls (the second image in figure 5(b)). In contrast to the relatively long-lived clusters observed for longitudinal forcing, here a ‘kink-cluster’ became immediately unstable to an orientation transition, which resulted in the steady RP pattern of figure 5(a).

*Oblique forcing* ( $\varphi = 60^\circ$ ): For small  $\varepsilon$ , *oblique rolls* (OR) that were phase-locked with the underlying SU-8 structure were observed. This steady pattern became unstable to *KL*, which aggregated to form larger patches of kink clusters, similar to the longitudinal forcing case (figure 6(a)). With further increase in  $\varepsilon$  the kink clusters aligned parallel to gravity, resulting in

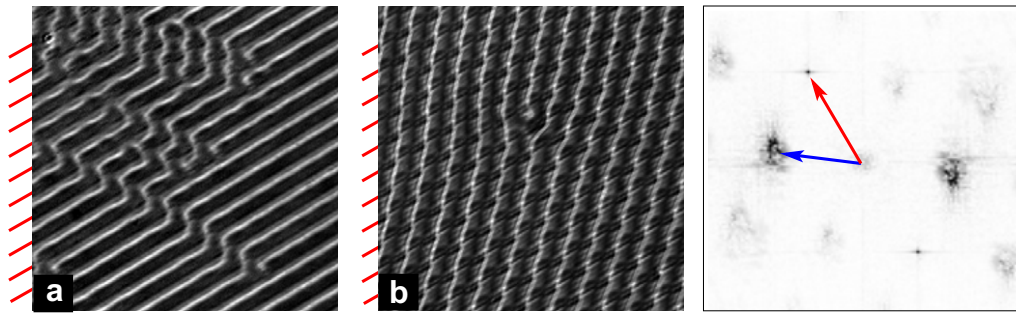


**Figure 6.** Low inclination patterns due to oblique forcing ( $\varphi = 60^\circ$ ). (a) Kinks at  $\theta = 10^\circ$  and  $\varepsilon = 0.42$ . (b) MLR at  $\theta = 10^\circ$  and  $\varepsilon = 1.57$ . (c) Fourier transform of (b) with arrows for the forcing mode  $\mathbf{q}_0$  (red) and the largest side mode  $\mathbf{q}_1$  (blue). The red lines in (a) and (b) mark the locations of the SU-8 ridges.

*modulated LR* (MLR) as shown in figure 6(b). The tendency of the system to form (modulated) LR with increasing  $\varepsilon$  has already been reported earlier for RP. The MLR were slightly inclined with respect to the in-plane gravity component as can also be seen in the corresponding Fourier transform in figure 6(c). The Fourier mode  $\mathbf{q}_1$  is not horizontal but has a small finite component in the  $y$ -direction. Similar oblique rolls have also been observed in other anisotropic pattern forming systems, for example in electroconvection [32, 33].

It is important to recall that for the oblique forcing the cell side walls were no longer parallel and perpendicular to the SU-8 ridges, but rather have angles of  $30^\circ$  and  $60^\circ$  to them. Since straight rolls tend to align perpendicular to the lateral side walls [3, 34–36], the side wall destabilized the forced straight rolls (that have angles of  $60^\circ$  and  $30^\circ$  to them) and led to phase defects of the straight roll pattern as was reported by McCoy *et al* [13]. As a result, kink structures that were induced by the lateral boundaries were observed even in the horizontal case instead of a VP. This is similar to the forced horizontal convection studied by McCoy *et al* [13, 15].

### 6.3. Intermediate inclination angles

*Longitudinal forcing* ( $\varphi = 0^\circ$ ): For inclination angles  $28^\circ < \theta < 72^\circ$ , forced LR became unstable to uniformly drifting undulations (UN) as shown in figure 7. This state, which was also observed for unforced ILC [26], is characterized by the modes  $\mathbf{q}_1 = q_f(1, s_y)$  and  $\mathbf{q}_2 = q_f(1, -s_y)$ , where  $s_y$  decreased with increasing inclination angle from  $s_y = 0.47$  for  $\theta = 30^\circ$  to  $s_y = 0.25$  for  $\theta = 65^\circ$  (taken at undulation onset). While unforced UN were often defect turbulent (undulation chaos) [18, 26], forced UN were mostly ordered and only rarely perturbed by fast traveling defects. This fact, together with the previously mentioned shift of the instability line to higher values of  $\varepsilon$ , (section 5) is a clear indication of the stabilizing effect of forcing.

Undulations slowly drifted in the uphill direction with increasing speed as the LSF intensified (increasing  $\theta$  and increasing  $\varepsilon$ ). The drift velocity ranged from  $v_{\text{drift}} \approx 0.13d/\tau_\kappa$  (at  $\theta = 50^\circ$  and  $\varepsilon = 0.1$ ) to  $v_{\text{drift}} \approx 0.74d/\tau_\kappa$  (at  $\theta = 65^\circ$  and  $\varepsilon = 0.1$ ). When  $\varepsilon$  increased, dislocations started to occur. These dislocations gradually turned the UN state into a chaotic state of *crawling rolls* (CR; figure 8(a)), similar to the one observed in the unforced cell [18].

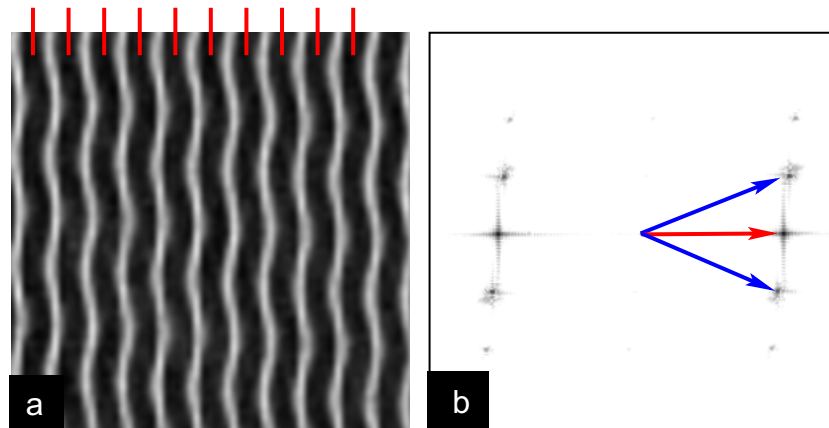


**Figure 7.** Ordered UN (a) and the corresponding Fourier transform (b) taken at  $\theta = 55^\circ$  and  $\varepsilon = 0.28$ . The red arrow in (b) marks the forced mode, while the two side modes  $\mathbf{q}_1$  and  $\mathbf{q}_2$  are marked in blue. The short red lines mark the location of the SU-8 ridges.

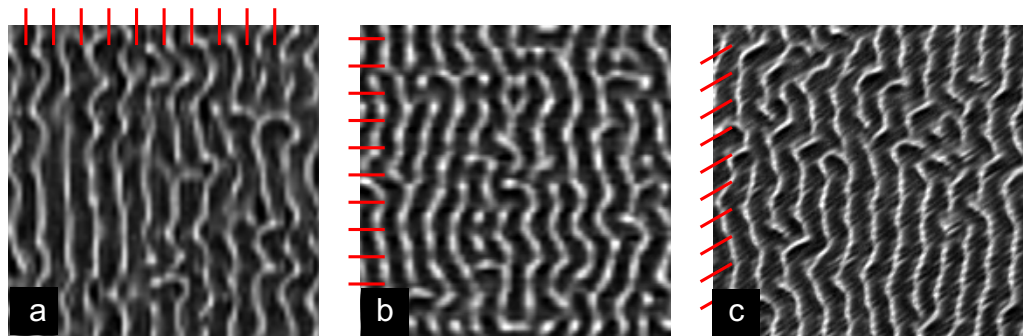


**Figure 8.** CR for longitudinal forcing (a) (at  $\theta = 45^\circ$ ,  $\varepsilon = 0.79$ ) and similar states for transverse forcing (b) (at  $\theta = 30^\circ$ ,  $\varepsilon = 0.69$ ) and the oblique forcing case (c) (at  $\theta = 20^\circ$ ,  $\varepsilon = 0.61$ ). Red stripes mark the location of the SU-8 ridges. See also movie 3 for (a) and movie 4 for (b) in the supplementary material (available from [stacks.iop.org/NJP/14/053010/mmedia](http://stacks.iop.org/NJP/14/053010/mmedia)).

CR were also observed at relatively high  $\varepsilon$  both for transverse forcing (figure 8(b)) and for oblique forcing (figure 8(c)). Indeed, for high values of  $\varepsilon$ , the influence of the forcing weakened and the states of unforced ILC were observed.

*Transverse forcing* ( $\varphi = 90^\circ$ ): In this case, similar to the low inclination regime, the forcing enhanced the transverse modes, while the LSF supported the longitudinal modes. As a result, when the LSF became sufficiently strong with increasing  $\varepsilon$ , forced TR became unstable either to a *hexaroll pattern* (HR) when  $10 \lesssim \theta \lesssim 30^\circ$  or to a *bimodal pattern* (BM) when  $30^\circ \lesssim \theta \lesssim 75^\circ$  (figure 9). The HR pattern is named after a similar pattern found in centrifugal convection ([25, 37, 38]). In addition to the forcing wave vector  $\mathbf{q}_0$ , two other modes  $\mathbf{q}_1 = q_f(s_x, 0.5)$  and  $\mathbf{q}_2 = q_f(-s_x, 0.5)$  appeared, with  $s_x$  monotonically increasing from  $s_x = 0.66$  at  $\varepsilon = 0.038$  (onset of HR) to  $s_x = 0.80$  at  $\varepsilon = 0.155$  (onset of CR). All three wave vectors formed a resonant triad  $\mathbf{q}_0 = \mathbf{q}_1 + \mathbf{q}_2$ .

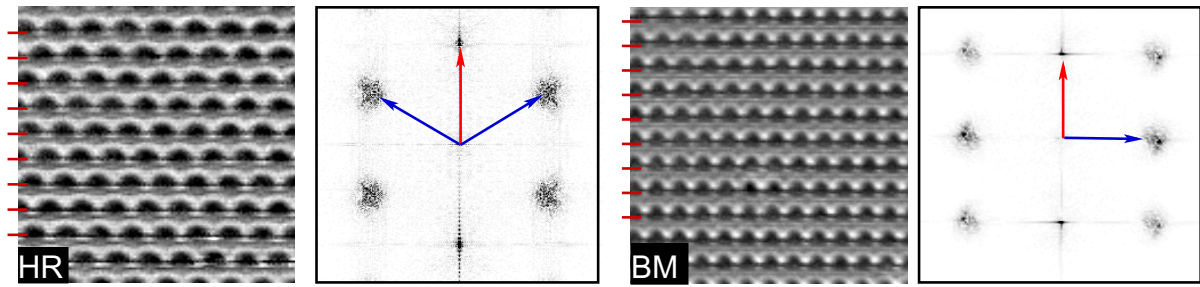


**Figure 9.** Patterns due to a moderate inclination under transverse forcing and their Fourier transform. Left: HR (at  $\theta = 20^\circ$ ,  $\varepsilon = 0.12$ ). Right: BM pattern (at  $\theta = 60^\circ$ ,  $\varepsilon = 0.20$ ). Red stripes mark the SU-8 ridges.

BM patterns have the forcing wave vector  $\mathbf{q}_0$  and an orthogonal mode  $\mathbf{q}_1 = q_f(s, 0)$  with  $s$  varying in the range  $0.9 < s < 1.2$  for inclination angles  $35^\circ < \theta < 75^\circ$ . For unforced ILC a similar pattern occurred at a small strip in the direct vicinity of the codimension two point ( $\theta_{cd}$ ). Here, however, BM was the dominating pattern over a large region in the  $\theta$ - $\varepsilon$ -phase space (see figure 3(b)). It should also be noted that the BM state is rarely perturbed by localized amplitude and phase modulations.

A qualitatively similar pattern was also found in thermal centrifugal convection, where it was called the knot instability [25, 37, 38]. The similarity between thermal centrifugal convection, on the one hand, where fluid motion between a cold inner and a warm outer cylinder is driven by centrifugal forces rather than gravity, and transverse forced ILC, on the other, is interesting. Both are anisotropic systems that develop LR with a preferred orientation at convection onset (at least for sufficiently large anisotropy). In both systems, HR and bimodal/knot patterns appear as an instability of these rolls when the Rayleigh number (although slightly differently defined) is increased. The shape of the HR and the bimodal/knot convection is in both cases influenced by a large-scale flow, which is caused by the inclination in forced ILC and by Coriolis forces in the centrifugal convection. For example, in both cases, the *knots* are not symmetric along the lines of cold down-flow or warm up-flow, but are shifted to an asymmetric position, which is in contrast to the *knots* observed in planar RBC at large Prandtl numbers [39]. It is furthermore, very interesting to note that HR and bimodal/knot patterns turn into a state of phase turbulence (CR) when the Rayleigh number is increased further.

*Oblique forcing* ( $\varphi = 60^\circ$ ): For inclination angles  $10^\circ < \theta < 53^\circ$  stationary oblique rolls with wave vector  $\mathbf{q}_0 = \mathbf{q}_f$  became unstable to an *oblique bimodal pattern* (OB). Here, the pattern can be described by  $\mathbf{q}_0$  and a second mode  $\mathbf{q}_1$  which depends on the inclination angle. The plot in figure 10(c) shows its modulus ( $|\mathbf{q}_1|$ ; blue triangles, the left y-axis) and its angle  $\alpha$  with respect to  $\mathbf{q}_0$  (green bullets, the right y-axis) as a function of  $\theta$ . Both quantities grow from  $|\mathbf{q}_1| \approx 0.8q_f$  and  $\alpha \approx 70^\circ$  at  $\theta = 15^\circ$  to  $|\mathbf{q}_1| \approx 1.1q_f$  and  $\alpha \approx 120^\circ$  at  $\theta = 85^\circ$ . As shown in figure 10(d), for large inclination angles a higher order mode  $\mathbf{q}_2$  moves in such that  $\mathbf{q}_0 + \mathbf{q}_1 + \mathbf{q}_2 = 0$ . Therefore, in particular in the range  $60^\circ < \theta < 75^\circ$ , the pattern is hexagonal.

Oblique BM drifted slowly along the SU-8 ridges in the downhill direction with typical velocities of  $v_d \approx 0.5 - 0.9d/\tau_k$ . In addition, fast traveling phase and amplitude defects occurred with growing  $\varepsilon$ . The dynamics of these defects increased with increasing  $\varepsilon$ , leading to a local merging of adjacent structures and to a continuous transition to CR (figure 8(c)).



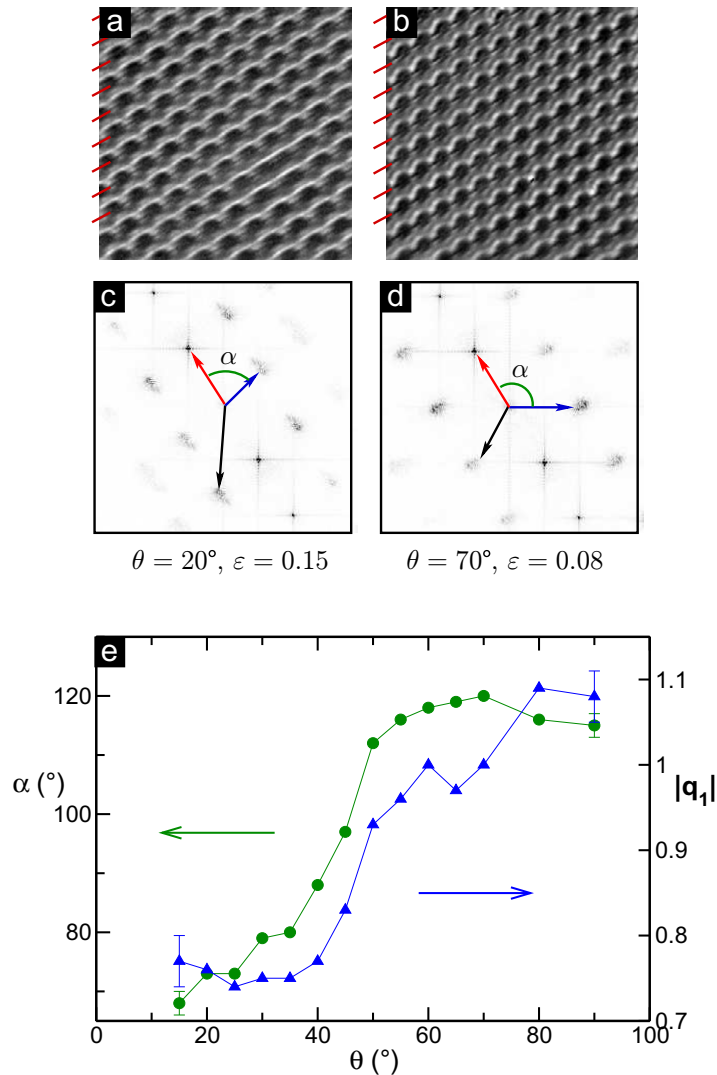


**Figure 10.** Patterns due to a moderate inclination under oblique forcing (a), (b) and their Fourier transform (c), (d). The left column (a), (c) shows OB at  $\theta = 20^\circ$  and  $\epsilon = 0.15$ . The right column (b), (d) shows a similar pattern at  $\theta = 70^\circ$  and  $\epsilon = 0.08$ . Red stripes in (a) and (b) mark the location of the SU-8 ridges. The red and blue arrows in (c) and (d) mark the forcing mode  $\mathbf{q}_0$  and the mode  $\mathbf{q}_1$ , respectively. A higher order mode  $\mathbf{q}_2$  exists for small inclination angles (black arrow) which turns for large inclination such that it forms with  $\mathbf{q}_0$  and  $\mathbf{q}_1$  a nearly hexagonal symmetry. Panel (e) shows the development of the modulus  $|\mathbf{q}_1|$  (blue triangles) and its angle  $\alpha$  with respect to  $\mathbf{q}_0$  (green bullets) as a function of the inclination angle  $\theta$ . Error bars are shown for the first and last points and give the uncertainty of determining the exact position of  $\mathbf{q}_1$ .

#### 6.4. Large inclination angles

For inclination angles close to  $\theta_{cd}$  and larger, the forced straight rolls became unstable at low or even negative  $\epsilon$  and the patterns that occurred were highly dynamical.

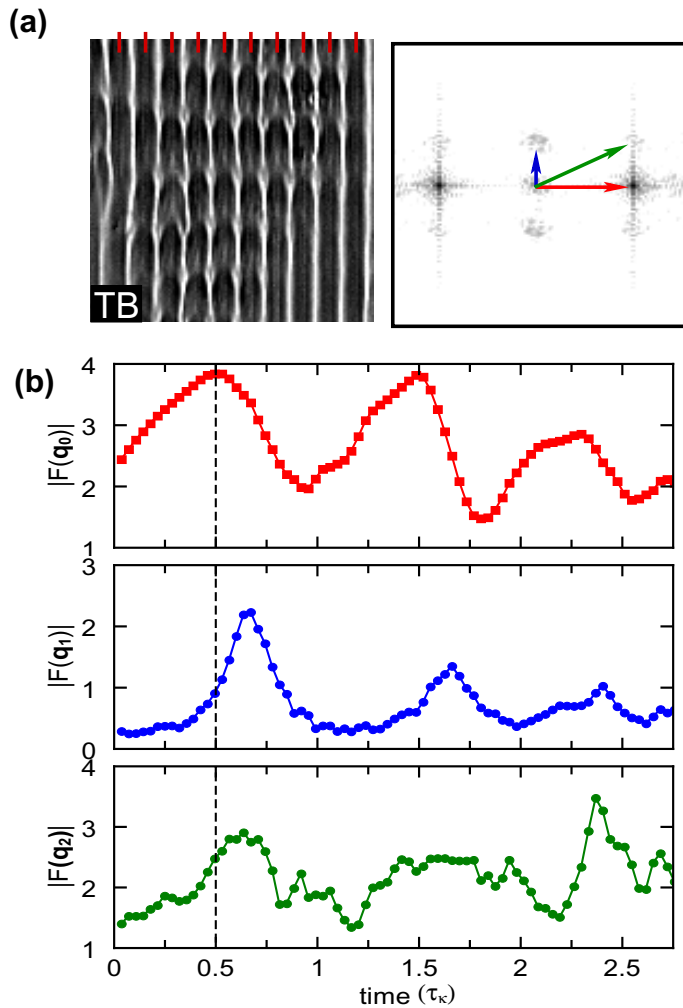


**Figure 11.** (a) Array of TB and its Fourier transform (TB, at  $\theta = 80^\circ$ ,  $\varepsilon = 0.17$ ). Red stripes show the SU-8 ridges. The red arrow in the Fourier transform marks the forcing mode  $\mathbf{q}_0$ , the blue arrow the side mode  $\mathbf{q}_1$  and the green arrow the mode  $\mathbf{q}_2$ . (b) Fourier amplitudes of the three modes  $\mathbf{q}_0$  (top),  $\mathbf{q}_1$  (middle) and  $\mathbf{q}_2$  (bottom) as a function of time for three consecutive bursts. The time is given in units of the vertical thermal diffusion time  $\tau_\kappa$ . The dashed vertical lines mark the time at which the snapshot in (a) was taken. The units of the y-axis are arbitrary units. See movie 5 in the supplementary material (available from [stacks.iop.org/NJP/14/053010/mmedia](http://stacks.iop.org/NJP/14/053010/mmedia)).

*Longitudinal forcing* ( $\varphi = 0^\circ$ ): In the longitudinal forcing case, we observed patterns similar to those found in unforced ILC [18]. The dynamics and the extent of these states in parameter space (figure 3) differed, however. For example, *transverse bursts* (TB) (see figure 11 and movie 5 in the supplementary material (available from [stacks.iop.org/NJP/14/053010/mmedia](http://stacks.iop.org/NJP/14/053010/mmedia))), which for unforced ILC occurred only in a small region close to the codimension two point ( $\theta_{cd}$ ), were observed here for  $72^\circ < \theta < 82^\circ$ .

As described elsewhere [28], TB occurred spontaneously as a periodic modulation of LR in the  $y$ -direction as shown in figure 11(a). The spatial periodicity in the longitudinal direction was

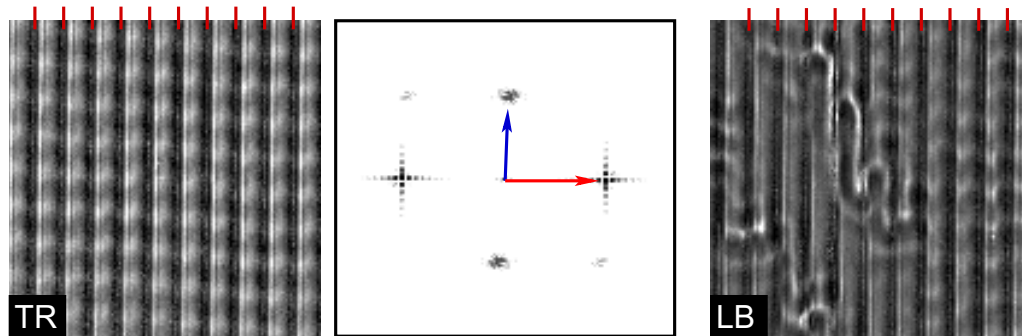


**Figure 12.** Left: TR at  $\theta = 85^\circ$  and  $\varepsilon = 0.10$ . Middle: Fourier transform of TR. Right: LB at  $\theta = 85^\circ$  and  $\varepsilon = 0.2$ . See movie 6 in the supplementary material (available from [stacks.iop.org/NJP/14/053010/mmedia](http://stacks.iop.org/NJP/14/053010/mmedia)).

about twice the forcing wave length (wave vector  $\mathbf{q}_1 = (0, 0.5)q_f$ , blue arrow in figure 11(a)), whereas the periodicity in the transverse direction is the forcing wave length (wave vector  $\mathbf{q}_0 = (q_f, 0)$ , red arrow in figure 11(a)). These bursts were localized and appeared in small regions with three to six modulation periods ( $2\pi/q_1$ ) in the  $x$ -direction and two to three periods ( $2\pi/q_f$ ) in the  $y$ -direction. In addition to  $\mathbf{q}_0$  and  $\mathbf{q}_1$  there is also a third resonant mode  $\mathbf{q}_2$  with  $\mathbf{q}_2 = \mathbf{q}_0 + \mathbf{q}_1$ .

Figure 11(b) shows the temporal evolution of the amplitudes of the forcing mode  $\mathbf{q}_0$  (top graph), the transverse mode  $\mathbf{q}_1$  (middle graph) and  $\mathbf{q}_2$  (bottom graph) for three consecutive bursts.

At  $t = 0$  LR were present so that the amplitude of  $\mathbf{q}_1$  is nearly zero. The appearance of a burst led first to an increase of the amplitude of  $\mathbf{q}_0$  followed by an increase of the amplitude of  $\mathbf{q}_1$ . The forced mode reached a maximal amplitude after about  $0.50 t_\kappa$  and started to decrease from this point onwards. The amplitude of  $\mathbf{q}_1$  continued to increase and reached a maximum at  $t = 0.65 t_\kappa$  before it also decayed. At this point, the whole flow pattern became unstable and was temporarily destroyed, resulting in low Fourier amplitude of  $\mathbf{q}_0$ ,  $\mathbf{q}_1$  and  $\mathbf{q}_2$ . We wish to point out here that the amplitude of  $\mathbf{q}_0$  never reaches zero since a Fourier transform was applied to an area that was not fully covered by bursts, but where also LR remained stable over the considered time range (e.g. the bottom right corner of figure 11(a)). This behavior is very similar to that observed in unforced ILC [28].

The three plots in figure 11(b) suggest a resonant coupling between  $\mathbf{q}_0$ ,  $\mathbf{q}_1$  and  $\mathbf{q}_2$ , such that TB rely on an instability of LR. This three-mode resonance would also explain why in the forced case the inclination range, for which TB were found, is large in comparison to the unforced case, where TB were observed only close to  $\theta_{cd}$ .

For even larger inclination angles ( $82^\circ \leq \theta \leq 90^\circ$ ), *transverse rolls* (TR) were found for small  $\varepsilon$ . These rolls were modulated in the horizontal direction by the SU-8 texture. Hence, in the Fourier transform (figure 12) the forced mode  $\mathbf{q}_0$  (red arrow) and the transverse mode  $\mathbf{q}_1$  (blue arrow) are visible. The second mode has a modulus of  $|\mathbf{q}_1| \approx 0.84q_f = 2.86/d$  which is close to the theoretically predicted value of TR in the unforced ILC  $q_{\text{theory}} \approx 2.82/d$  (blue dashed-dotted curve in figure 2(b)).

As  $\varepsilon$  increased, TR became locally unstable to *longitudinal bursts* (LB), similar to the ones found in unforced ILC [18] (right image in figure 12 and movie 6 in the supplementary

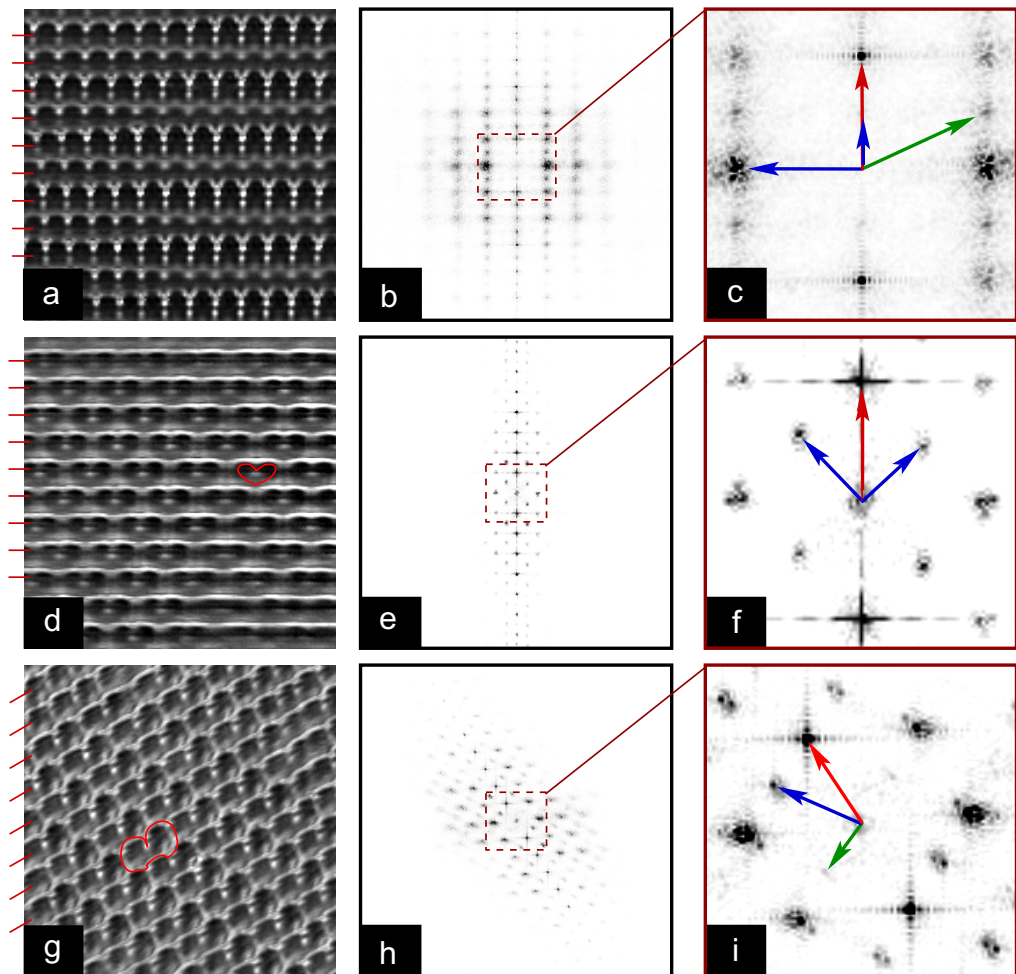


**Figure 13.** SP (a), HP (d) and PZ pattern (g), their corresponding Fourier spectra (b), (e), (h) and the central section of the Fourier spectra (c), (f), (i). Here the blue arrows mark the first order modes of the underlying lattice, the red arrow is the forced mode and the green vector is a higher order mode. See movie 7 for SP and movie 8 for HP in the supplementary material (available from [stacks.iop.org/NJP/14/053010/mmedia](http://stacks.iop.org/NJP/14/053010/mmedia)).

material (available from [stacks.iop.org/NJP/14/053010/mmedia](http://stacks.iop.org/NJP/14/053010/mmedia))). There, the amplitude of the longitudinal modulation is increased locally, while the transverse amplitude is damped for a short time. These bursts quickly extended in the longitudinal direction for a few wave lengths and faded away again.

*Transverse forcing* ( $\varphi = 90^\circ$ ): Whereas for small inclination angles ( $\theta < 55^\circ$ ) BM became unstable to CR, for larger  $\theta$  the fascinating *scepter pattern* (SP) was observed (shown in figure 13). This pattern consisted of scepter-like structures located at the sites of a rectangular lattice with side lengths  $\lambda_f$  and  $2\lambda_f$  with  $\lambda_f = 2\pi/q_f$ .

The SP was highly dynamical (see movie 7 in the supplementary material). The head of a scepter moved quickly to the right and to the left with a typical time scale of  $\approx 0.18 t_\kappa$ . In addition, phase defects traveling through the cell transformed the SP temporally (for  $\approx 4-5 t_\kappa$ )

back into BM. It is worth noting that in the same region of phase space, both in the unforced and in the longitudinal forcing case, one observed turbulent TB. As shown in figure 11, TB are characterized by exactly the same sub-harmonic transverse wave vector  $\mathbf{q}_1 = q_f(0, 0.5)$  as the underlying rectangular lattice of SP. Moreover, a close comparison between the bursts and the ‘scepters’ (figures 11 and 13(a)) shows a close resemblance of the two patterns. While TB was a transient state with a characteristic time scale of less than  $1 t_\kappa$ , SP existed approximately 10 times longer until a defect temporarily destroyed it. Thus, one can interpret the SP state as a stabilized version of the transverse bursts.

At inclination angles  $80^\circ < \theta < 90^\circ$ , the superlattice *heart pattern* (HP) was observed. It consisted of small ‘heart’-shaped elements, which were located at the sites of a square lattice (oriented at  $45^\circ$  with respect to the SU-8 stripes). The underlying Fourier lattice was spanned by the wave vectors  $\mathbf{q}_1 = q_f(0.5, 0.5)$  and  $\mathbf{q}_2 = q_f(-0.5, 0.5)$ , which together with the forcing wave vector fulfill the resonant triad condition  $\mathbf{q}_0 = \mathbf{q}_1 + \mathbf{q}_2$ . The dynamics of HP is slower than that of SP, and is characterized by patches of HP fading and reappearing with a time scale of the order of  $2-5 \tau_\kappa$  (see movie 8 in the supplementary material (available from [stacks.iop.org/NJP/14/053010/mmedia](http://stacks.iop.org/NJP/14/053010/mmedia))).

We can compare HP with the *switching diamond panes* (SDP) that were found in the unforced ILC by Daniels *et al* [18]. These are spatio-temporal chaotic roll structures that consist of large patches, aligned  $45^\circ$  and  $-45^\circ$  to the direction of inclination. The patches are thin and elongated and have rolls with a large amplitude, whereas, outside these patches, the amplitude is reduced. Because of their similar shapes and dynamics, one can imagine that HP are stabilized SDP.

*Oblique forcing* ( $\varphi = 60^\circ$ ): A superlattice state was also found for the oblique forcing case. Here, for inclination angles  $\theta > 75^\circ$ , oblique HR became unstable at large values of  $\varepsilon$  to a *pretzel pattern* (PZ), shown in figure 13(g). Small elements that are shaped like a pretzel are located on a rhombic lattice. The corresponding reciprocal vectors are  $\mathbf{q}_1 = -0.5 q_f(\cos(60^\circ), \sin(60^\circ))$  (green arrow in figure 13(b)) and  $\mathbf{q}_2 = \mathbf{q}_0 + \mathbf{q}_1$  (blue arrow in figure 13) as shown in the Fourier transform.

## 7. Discussion and conclusion

Motivated by the fact that naturally driven pattern forming systems often consist of intrinsic and externally imposed symmetry breaking mechanisms, we have investigated experimentally the combined effect of two independent symmetry breaking mechanisms on an otherwise isotropic system. Thermal convection of a thin fluid layer heated on one side and cooled on the other was chosen as a model system. The externally imposed symmetry breaking mechanisms were a unidirectional shear flow, caused by inclining the fluid layer, and lithographically fabricated, periodic surface corrugations of the warm plate. The latter breaks both the rotational invariance and the translational symmetry. In our investigation, the relative strength and the relative orientation of both symmetry breaking mechanisms were tuned, thus allowing for a broad variety of 2D forcing scenarios.

Our exploration focused on selected  $\theta$ - $\varepsilon$  phase diagrams in the  $\theta$ - $\varepsilon$ - $\varphi$  parameter space. Specifically, we chose forcing angles that correspond to the most generic symmetries for lattice patterns:  $\varphi = 0^\circ$  (parallel stripes),  $60^\circ$  (hexagons), and  $90^\circ$  (squares). In all three phase diagrams we could distinguish three different  $\theta$ -regions. For small  $\theta$ , straight rolls became unstable at rather large  $\varepsilon$ . As a result, we observed VP and kinks for longitudinal forcing, RP for transverse

forcing as well as oblique kinks and modulated LR for oblique forcing. For moderate  $\theta$ , straight rolls became unstable to simple slowly drifting patterns that consisted of only two or three different modes. These were UN for longitudinal forcing, HR and BP for transverse forcing and OB for oblique forcing. All these patterns turned continuously into CR when  $\varepsilon$  was increased. For large  $\theta$  (close to and larger than  $\theta_{cd}$ ) straight rolls became unstable at rather small  $\varepsilon$ . The instability resulted in highly dynamical transverse bursts or TR for longitudinal forcing, SP and HP for transverse forcing and PZ pattern for oblique forcing.

In general, we observed a strong stabilizing effect due to spatial periodic forcing. As an example, for longitudinal forcing the region in the phase diagram where steady convection rolls are stable was extended in comparison with the unforced ILC. Also, a noticeable reduction of spatio-temporal chaos in dynamical states was found. Examples of the latter are the VP (forced ILC), which can be considered as a stabilized version of subharmonic oscillations (unforced ILC), ordered UN (forced ILC) in contrast to undulation chaos (unforced ILC), SP (forced ILC) as stabilized transverse bursts (unforced ILC and  $\varphi = 0$  forcing) or HP (forced ILC) that can be associated with SDP (unforced ILC). Furthermore, the number of defects that occurred in the UN was reduced in the forced case in comparison with the unforced case (see also [26]). Since the degree of stabilization depends on the forcing amplitude  $\delta$  one can speculate that an increase of  $\delta$  would further reduce the number of defects and thus might also shift the onset for CR to larger  $\varepsilon$ .

This is just one example of how the shape of the phase diagram depends on  $\delta$ . Indeed, all three phase diagrams have to converge for  $\delta \rightarrow 0$  towards the unforced ILC-phase diagram (figure 4 of [18]). Therefore, for small and intermediate inclination angles, an increase of  $\delta$  would also stabilize forced rolls and shift their instability lines towards larger  $\varepsilon$ . But we have also seen in the case of TB that the forcing can actually destabilize the roll solution due to a resonant coupling of longitudinal and transverse modes when  $\theta$  is close to  $\theta_{cd}$ . In this range, increasing  $\delta$  might therefore lead to reduced stability of straight rolls. We also wish to point out that speculations on how much the phase diagrams depend on  $\delta$  are only valid when the forced wavelength is sufficiently close to the critical wavelength of the system. It was shown in simulations of horizontal forced convection [40] that for certain ratios  $q_f/q_c < 0.75$  an increase of  $\delta$  can lead to reduced stability of the forced rolls (see, e.g., figure 5 of [40]).

We have also observed the tendency that forcing has a significant effect on patterns that occur at small values of the control parameter  $\varepsilon$ , while for larger  $\varepsilon$  the observed patterns were similar to that observed in unforced ILC. While at small  $\varepsilon$  the occurring straight rolls were all phase-locked with the forcing profile, the patterns at larger  $\varepsilon$  became more similar to that observed in the unforced system such as LR for small inclination angles and CR for larger ones. In these examples the shape and dynamics of the patterns depended at most only weakly on the specific forcing case, i.e. the specific  $\varphi$ .

The patterns that occurred due to forcing for small  $\varepsilon$  and  $\theta < 70^\circ$  consisted of modes that continuously grew out of a steady roll pattern, following a supercritical (forward) bifurcation (VP, UN, HR, BM, OB, OX). These patterns show very weak dynamics. In contrast to this observation, it was shown that breaking the symmetry in a pattern forming system can have a more dramatic effect if some of the solutions of the symmetric system undergo a subcritical (backward) bifurcation (see e.g. [41, 42]). In a system with broken  $D_4$ -symmetry, for example, the interaction of two modes can lead to heteroclinic cycles with some of the fixed points having infinite amplitudes. In general, the occurrence of periodic and chaotic bursts can be explained by

such a mechanism. However, this mechanism needs to be modified to allow for the description of spatially localized bursts as reported here (TB, LB).

A question one might ask is whether the exact shape of the surface profile of the warm plate has a significant influence on the patterns or the shape of the phase diagrams. For small  $\varepsilon$  when the horizontal variation of the temperature and flow field can be sufficiently described by only a very few Fourier modes, it was shown that an approximation of the surface profile of the warm plate by its first Fourier mode (resulting in a single forcing parameter  $\delta$ ) is sufficient to calculate correctly the convection amplitude of straight forced rolls [16, 21]. For larger  $\varepsilon$ , higher Fourier modes of the flow and temperature field become important and are most likely influenced by the higher modes of the forcing texture. Therefore it is likely that at larger  $\varepsilon$  the exact shape of the forcing pattern, i.e. *the surface corrugation of the warm plate*, becomes important. However, more theoretical and experimental investigations are necessary to answer this question quantitatively.

Since the up–down symmetry (‘Boussinesq symmetry’) with respect to reflection at the midplane of the convection layer was broken (only the warm plate was structured), most of the patterns did not show a symmetry regarding inversion of the cold and warm regions. Furthermore, many of these patterns consisted of three modes that built a resonant triad, where often the ‘natural’ selected wave vectors and the externally imposed periodicity were both represented in the patterns. Examples include VP, HR and HP. The existence of these triads allows for quadratic interactions in the amplitude equations for the Fourier modes.

The large variety of different patterns presented in this paper demonstrates the complex interaction between only two symmetry breaking mechanisms in a rather simple hydrodynamical system. The underlying processes and mode interactions that lead to this variety are far from understood and demand further experimental and theoretical investigation.

## Acknowledgments

We thank Professor Werner Pesch for providing us the code to calculate the onset of straight rolls of different angles in ILC, for his valuable advice and for numerous fruitful discussions. We also thank Professor Jeff Moehlis for discussions and very useful comments.

## References

- [1] Cross M C and Hohenberg P C 1993 Pattern formation outside equilibrium *Rev. Mod. Phys.* **65** 851
- [2] Cross M and Greenside H 2009 *Pattern Formation and Dynamics in Nonequilibrium Systems* (Cambridge: Cambridge University Press)
- [3] Bodenschatz E, Pesch W and Ahlers G 2000 Recent developments in Rayleigh–Bénard convection *Annu. Rev. Fluid Mech.* **32** 709–78
- [4] Kessler M A and Werner B T 2003 Self-organization of sorted patterned ground *Science* **299** 380
- [5] Valentin C, d’Herbés J M and Poesen J 1999 Soil and water components of banded vegetation patterns *Catena* **37** 1–24
- [6] Tian W, Parker D J and Kilburn C A D 2003 Observation and numerical simulation of atmospheric cellular convection over mesoscale topography *Mon. Weather Rev.* **131** 222
- [7] Kuecken M and Newell A C 2005 Fingerprint formation *J. Theor. Biol.* **235** 71–83
- [8] Busse H F and Whitehead J A 1971 Instabilities of convection rolls in a high Prandtl number fluid *J. Fluid Mech.* **47** 305–20

- [9] Lowe M and Gollub J P 1985 Solitons and the commensurate–incommensurate transition in a convecting nematic fluid *Phys. Rev. A* **31** 3893
- [10] Míguez D G, Nicola E M, Munuzuri A P, Casademunt J, Sagués F and Kramer L 2004 Traveling-stripe forcing generates hexagonal patterns *Phys. Rev. Lett.* **93** 048303
- [11] Dolnik M, Berenstein I, Zhabotinsky A M and Epstein I R 2001 Spatial periodic forcing of Turing structures *Phys. Rev. Lett.* **87** 238301
- [12] Berenstein I, Yang L, Dolnik M, Zhabotinsky A M and Epstein I R 2003 Superlattice Turing structures in a photosensitive reaction–diffusion system *Phys. Rev. Lett.* **91** 058302
- [13] McCoy J H, Brunner W, Pesch W and Bodenschatz E 2008 Self-organization of topological defects due to applied constraints *Phys. Rev. Lett.* **101** 254102
- [14] Cakmur R V, Egolf D A, Plapp B B and Bodenschatz E 1997 Bistability and competition of spatiotemporal chaotic and fixed point attractors in Rayleigh–Bénard convection *Phys. Rev. Lett.* **79** 1853–6
- [15] McCoy J H 2007 Adventures in pattern formation: spatially periodic forcing and self-organization *PhD Thesis* Cornell University
- [16] Seiden G, Weiss S, McCoy J, Pesch W and Bodenschatz E 2008 Pattern forming system in the presence of different symmetry-breaking mechanisms *Phys. Rev. Lett.* **101** 214503
- [17] Weiss S 2009 Pattern formation in spatially forced thermal convection *PhD Thesis* Georg-August-Universität Göttingen
- [18] Daniels K, Plapp B and Bodenschatz E 2000 Pattern formation in inclined layer convection *Phys. Rev. Lett.* **84** 5320–3
- [19] Kurzweg U H 1970 Stability of natural convection within an inclined channel *J. Heat Trans.* **14** 190
- [20] Clever R M 1973 Finite amplitude longitudinal convection rolls in an inclined layer *J. Heat Trans.* **95** 407–8
- [21] Pesch W 2005 Convection with modulation *Technical Report* (unpublished)
- [22] de Bruyn J R, Bodenschatz E, Morris S W, Trainoff S, Hu Y, Cannell D S and Ahlers G 1996 Apparatus for the study of Rayleigh–Bénard convection in gases under pressure *Rev. Sci. Instrum.* **67** 2043
- [23] Trainoff S P and Cannell D S 2002 Physical optics treatment of the shadowgraph *Phys. Fluids* **14** 1340–63
- [24] Bryce Plapp B 1997 Spiral pattern formation in Rayleigh–Bénard convection *PhD Thesis* Cornell University
- [25] Brausch O 2001 Rayleigh–Bénard Konvektion in verschiedenen isotropen und anisotropen Systemen *PhD Thesis* Universität Bayreuth
- [26] Daniels K, Brausch O, Pesch W and Bodenschatz E 2008 Competition and bistability of ordered undulations and undulation chaos in inclined layer convection *J. Fluid Mech.* **597** 261–82
- [27] Clever R M and Busse F H 1977 Instabilities of longitudinal rolls in an inclined layer *J. Fluid Mech.* **81** 107
- [28] Daniels K E, Wiener R J and Bodenschatz E 2003 Localized transverse bursts in inclined layer convection *Phys. Rev. Lett.* **91** 114501
- [29] Busse F H 1978 Nonlinear properties of convection *Rep. Prog. Phys.* **41** 1926–67
- [30] Porter J and Silber M 2004 Resonant triad dynamics in weakly damped Faraday waves with two-frequency forcing *Physica D* **190** 93–114
- [31] Topaz C M, Porter J and Silber M 2004 Multifrequency control of Faraday wave patterns *Phys. Rev. E* **70** 066206
- [32] Ribotta R, Joets A and Lei L 1986 Oblique roll instability in an electroconvective anisotropic fluid *Phys. Rev. Lett.* **56** 1595–7
- [33] Dennin M, Cannell D S and Ahlers G 1998 Patterns of electroconvection in a nematic liquid crystal *Phys. Rev. E* **57** 638
- [34] Cross M C 1982 Ingredients of a theory of convective textures close to onset *Phys. Rev. A* **25** 1065–76
- [35] Hu Y, Ecke R and Ahlers G 1995 Convection for Prandtl numbers near 1: dynamics of textured patterns *Phys. Rev. E* **51** 3263–79
- [36] Liu J and Ahlers G 1996 Spiral-defect chaos in Rayleigh–Bénard convection with small Prandtl numbers *Phys. Rev. Lett.* **77** 3126–9
- [37] Auer M, Busse F H and Clever R M 1995 Three-dimensional convection driven by centrifugal buoyancy *J. Fluid Mech.* **301** 371–82



- [38] Jaletzky M and Busse F H 2000 New pattern of centrifugally driven thermal convection *Proc. Natl Acad. Sci. USA* **97** 5060
- [39] Busse F H and Clever R M 1979 Instabilities of convection rolls in a fluid of moderate Prandtl number *J. Fluid Mech.* **91** 319
- [40] Freund G, Pesch W and Zimmermann W 2011 Rayleigh–Bénard convection in the presence of spatial temperature modulations *J. Fluid. Mech.* **673** 318–48
- [41] Moehlis J and Knobloch E 1998 Forced symmetry breaking as a mechanism for bursting *Phys. Rev. Lett.* **80** 5329–32
- [42] Moehlis J and Knobloch E 2000 Bursts in oscillatory systems with broken D4 symmetry *Physica D: Nonlinear Phenom.* **135** 263–304